Article

Patterns

A method to establish functional vagus nerve topography from electro-neurographic spontaneous activity

Highlights

- A functional imaging method for peripheral nerves has been proposed
- Our method employs spontaneous physiological signals to perform function localization
- Anatomical information can be included in the method to obtain more accurate results
- Our method is data efficient and robust when considering several kinds of noise and artifacts

Authors

Andrea Pitzus, Simone Romeni, Fabio Vallone, Silvestro Micera

Correspondence

silvestro.micera@epfl.ch

In brief

Electrical stimulation of the vagus nerve modulates the activity of vital organs and can treat many pathologies. Adverse effects could be avoided if we knew the location in the nerve section of the fibers communicating with different organs. We introduce a method to determine such locations using only recordings of spontaneous activity without altering any bodily functions. Such a method could be generalized to other parts of the nervous system and be used to produce personalized stimulation protocols.

Pitzus et al., 2022, Patterns *3*, 100615
November 11, 2022
https://doi.org/10.1016/j.patter.2022.100615

CellPress

Patterns

CellPress
OPEN ACCESS

Article

A method to establish functional vagus nerve topography from electro-neurographic spontaneous activity

Andrea Pitzus,[1,2,4] Simone Romeni,[3,4] Fabio Vallone,[1,4] and Silvestro Micera[1,3,5,*]

[1]The Biorobotics Institute and Department of Excellence in Robotics and AI, Health Interdisciplinary Center, Scuola Superiore Sant'Anna, Pontedera, Italy

[2]Department of Electrical and Electronic Engineering (DIEE), University of Cagliari, Cagliari, Italy

[3]Bertarelli Foundation Chair in Translational Neural Engineering, Center for Neuroprosthetics and Institute of Bioengineering, Ecole Polytechnique Federale de Lausanne, Lausanne, Switzerland

[4]These authors contributed equally

[5]Lead contact

*Correspondence: silvestro.micera@epfl.ch

https://doi.org/10.1016/j.patter.2022.100615

THE BIGGER PICTURE Electrical stimulation of the vagus nerve modulates the activity of internal organs and has the potential to treat many pathologies. Still, high selectivity is required because altering the functioning of off-target vital organs leads to severe adverse effects. Current steering can produce selective stimulation but requires knowing the functional organization of the target structure. Here, we introduce and test *in silico* a functional imaging method that allows localization in a nerve section of the fibers linked to several bodily functions. It employs spontaneous electroneurographic signals recorded from the implanted stimulation electrodes and a non-invasive physiological recording related to the target bodily function. The anatomy of the target structure is not required but can be incorporated to improve localization. The results are robust when considering different sources of noise and artifacts. Our method could be employed to determine personalized neuromodulation protocols.

Proof-of-Concept: Data science output has been formulated, implemented, and tested for one domain/problem

SUMMARY

Bioelectronic medicine is an emerging approach to treat many types of diseases via electrical stimulation of the autonomic nervous system (ANS). Because the vagus nerve (VN) is one of the most important nerves controlling several ANS functions, stimulation protocols based on knowledge of the functional organization of the VN are particularly interesting. Here, we proposed a method to localize different physiological VN functions by exploiting electro-neurographic signals recorded during spontaneous VN fibers activity. We tested our method on a realistic human cervical VN model geometry implanted via epineural or intraneural electrodes. We considered *in silico* ground truth scenarios of functional topography generated via different functional neural fibers activities covered by background noise. Our method accurately estimated the underlying functional VN topography by outperforming state-of-the-art methods. Our work paves the way for development of spatially selective stimulation protocols targeting multiple VN bodily functions.

INTRODUCTION

Bioelectronic medicine is an emerging approach with the aim of modulating visceral functions through electrical stimulation of the autonomic nervous system (ANS).[1,2] The vagus nerve (VN) is a particularly important stimulation target of the ANS because it takes part in controlling vital organs such as the heart, lungs, and digestive tract.[3] For this reason, stimulation should be sufficiently selective and grant modulation of the target function without altering other physiological functions. Several attempts to establish selective VN stimulation (VNS) have been performed by different research groups employing different techniques. The two main strategies are fiber-selective VNS and spatially selective VNS.[4]

In fiber-selective VNS, the different excitability properties of several fiber types are exploited to produce stimulation protocols that stimulate only one fiber type. This builds on evidence showing that the VN contains fibers belonging to different types[4] with fibers that carry out the same physiological function belonging to the same type. Two notable applications of this strategy are anodal block[5] and kilohertz block.[6] Although these fiber-selective stimulation methods can allow selective stimulation of large myelinated fibers versus small unmyelinated ones, they become increasingly ineffective when two target populations are similar (an afferent Aβ versus an efferent Aα population or two efferent Aα populations). They produce selectivity patterns that are very sensitive to the distance from the stimulation point.[7] To overcome the limitations of fiber-selective VNS, spatially selective stimulation protocols are currently the only viable solution. Efficient spatially selective stimulation protocols critically depend on the functional topography of the nerve, i.e., the spatial distribution of fibers accounting for different functions.

Although some anatomical analyses of the VN in humans and different animal models have been performed,[8,9] establishing a functional topography of the VN is technically challenging. Immunohistochemical analyses showed a spatial segregation at least between afferent and efferent fiber populations,[8] and the possibility to independently control bodily functions via stimulation protocols seems to suggest an organotopic organization of the VN.[10,11]

Electroneurographic (ENG) signals recorded through implanted electrodes in the peripheral nervous system have been used to localize functionally homogeneous clusters of fibers in motor nerves[12–14] and in the pig VN.[15] Wodlinger and Durand[12] used a beamforming (BF) method to produce spatial filters allowing localization of clusters of fibers targeting different muscle groups in the human femoral nerve. The BF method[12] can detect the activity of more than one cluster, but it cannot discriminate which part of the recovered functional distribution belongs to which source. For this reason, in their work, the authors of this study devise a ''calibration'' procedure where each muscle is contracted in turn and the location of the corresponding fiber cluster is determined. Vallone et al.[15] performed a study where cardiorespiratory-related functional clusters of fiber activity in the pig VN were localized by employing a measure called ''discriminative field potential'' (DFP). The DFP measure was based on an index, the discriminative index, quantifying the ability of an electrode to discriminate between different physiological conditions of the animal. This discriminative index was then weighted to the average values of lead field matrix entries representing the contribution of each fascicle to the recorded ENG signal at a given recording site. In this way, the DFP can determine which region of the nerve was most likely to be associated with a given cardiorespiratory function, thus quantifying the extent of spatial segregation between cardiorespiratory functional fiber activity clusters in a VN section.

All of these methods relied on modifications of neural activity by electrically stimulating motor nerves[12,14] or physiologically induced alterations of VN activity.[15] A promising alternative is electrical impedance tomography (EIT), which measures nerve impedance variations caused by spontaneous neural activity employing very-low-amplitude, high-frequency current injections not sufficient to substantially alter the physiological activity carried along the nerve.[16,17] However, it would be easier from a technical viewpoint to infer the functional topography of a nerve (e.g., the VN) from recorded spontaneous fiber activity without the need of any kind of current injection. For these reasons, here we propose a new method, which we call discriminative BF (DBF), by combining the strengths of the BF and DFP methods. Our approach employs discrimination indices built on VN activity markers able to identify different functional sources, thus isolating their contribution to the ENG signals. In this way, we do not need to alter the flow of physiological neural activity through the nerve, and we can, in principle, simultaneously identify an arbitrary number of sources, provided that an adequate discriminative index is defined for each of them. We then combined the discriminative indices with spatial filters calculated as in the BF method[12] to obtain a functional topography of the nerve.

We tested our new method on a realistic 2D nerve model geometry of the human cervical VN implanted via epineural or intraneural electrodes. We generated three different *in silico* experiments with increasing levels of complexity, starting from localization of single and multiple deterministic sources in Brownian background noise to concurrently active, physiologically plausible neural sources immersed in neural noise. We found that our new DBF method significantly outperforms the two already-existing methods: BF and DFP.

We also developed a computation pipeline to incorporate the fascicular morphology of the VN, showing an improvement of all localization methods with respect to missing morphological information.

RESULTS

Modeling approach and functional localization pipeline

The first step was to choose nerve geometry, electrode geometry, and material properties to build a model of the implanted nerve (Figures 1A–1C). In the present work, we performed simulations corresponding to the implants of a cuff electrode or of a transverse intrafascicular multichannel electrode (TIME).[18] In Figure 1D, we show the structural and generic geometric models. The structural model includes all fascicles in the nerve sections, whereas in the generic model, the nerve is a solid structure with the electrical properties of the extra-fascicular connective tissue. Using finite element modelling (FEM) on the chosen geometrical model of the nerve, we can obtain *in silico* a matrix containing the sensitivity of the potential recorded by each recording site to the neural signal from a specific nerve location (Figure 1E), called lead field matrix (LFM). In Figures 1F and 1G, we show how this matrix can be employed, together with discriminative indices associated with the recording sites, to compute a localization map (Figure 1H), which provides the likelihood that a given location of the nerve section contains the target function. Discriminative indices are computed here from the known features of the recorded spontaneous ENG signals; for example, from their correlation with a function-related physiological signal. Thus, the computations of neither the LFM nor the discriminative indices require performing nerve stimulation. In the present work, we quantified the performance of our localization algorithm through the localization error, defined as the

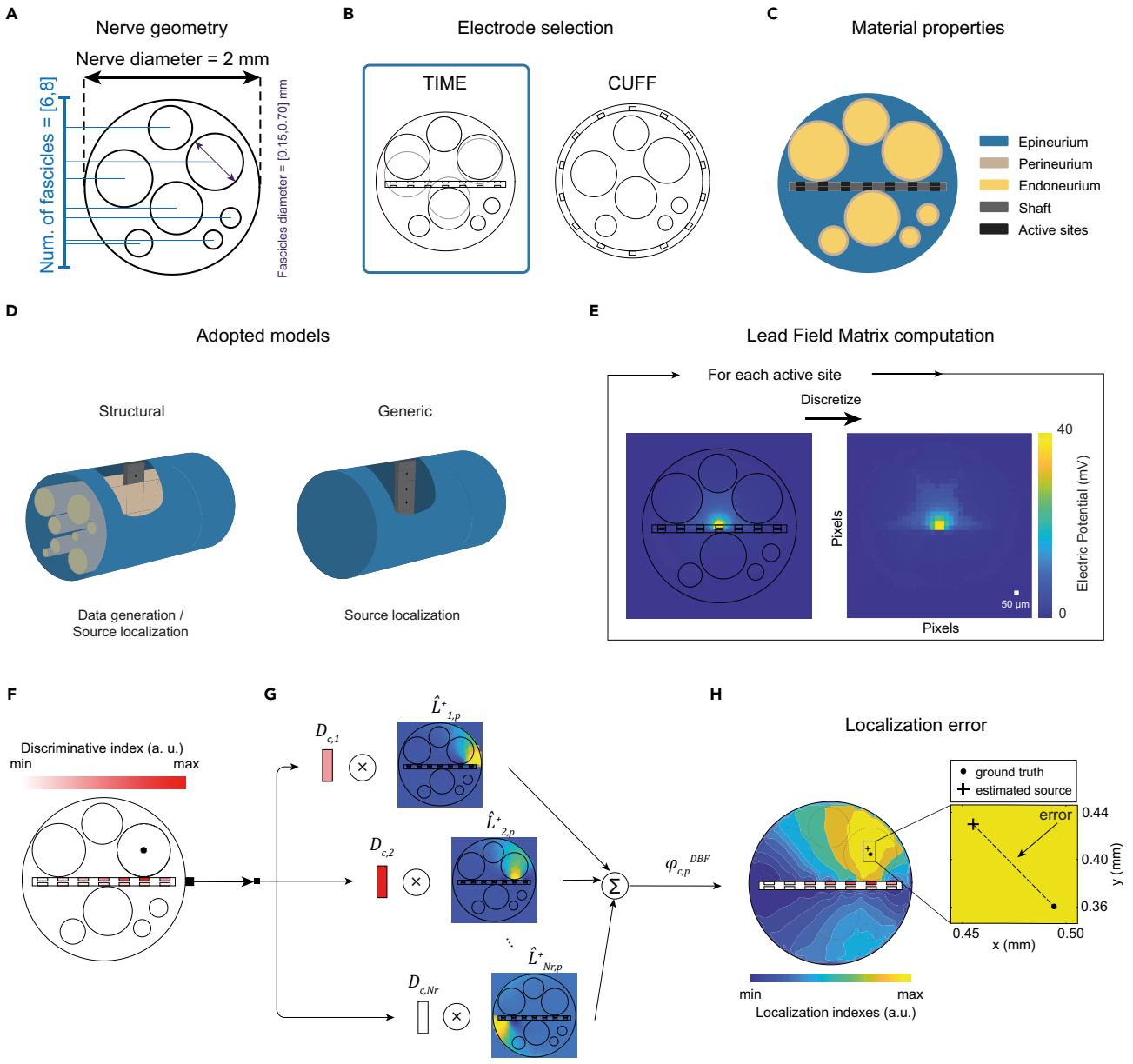

Figure 1. Function localization pipeline

(A) Generation of nerve geometry. Here we employ a nerve diameter of 2 mm, and a number of fascicles in (6, 8) with diameters in (0.15, 0.7) mm are placed in the nerve section.

(B) Generation of electrode geometry. Here, we show a TIME and a cuff electrode; in the case of TIME, fascicles are displaced so that no fascicles are pierced.

(C) Different domains constituting an implanted nerve section.

(D) Structural and generic geometric models. Recorded signal generation always employs the structural geometric model, whereas localization can be performed using either model.

(E) Left: FEM solution in terms of the electric potential map for unit current injected from each recording site. Right: discretization of the potential map. When flattened, it corresponds to a column of the lead field matrix (LFM).

(F) For each active site, a discriminative index is computed that determines the contribution of the corresponding LFM column (DFP) or pseudo-inverse LFM row (DBF) to the localization map (the black dot in the fascicle represents the source location).

(G) Weighting of the LFM components by the discriminative coefficients and summing up to obtain the localization map.

(H) Obtained localization map and localization error. The dot indicates the true location of the source, and the cross indicates the localization determined by the method.

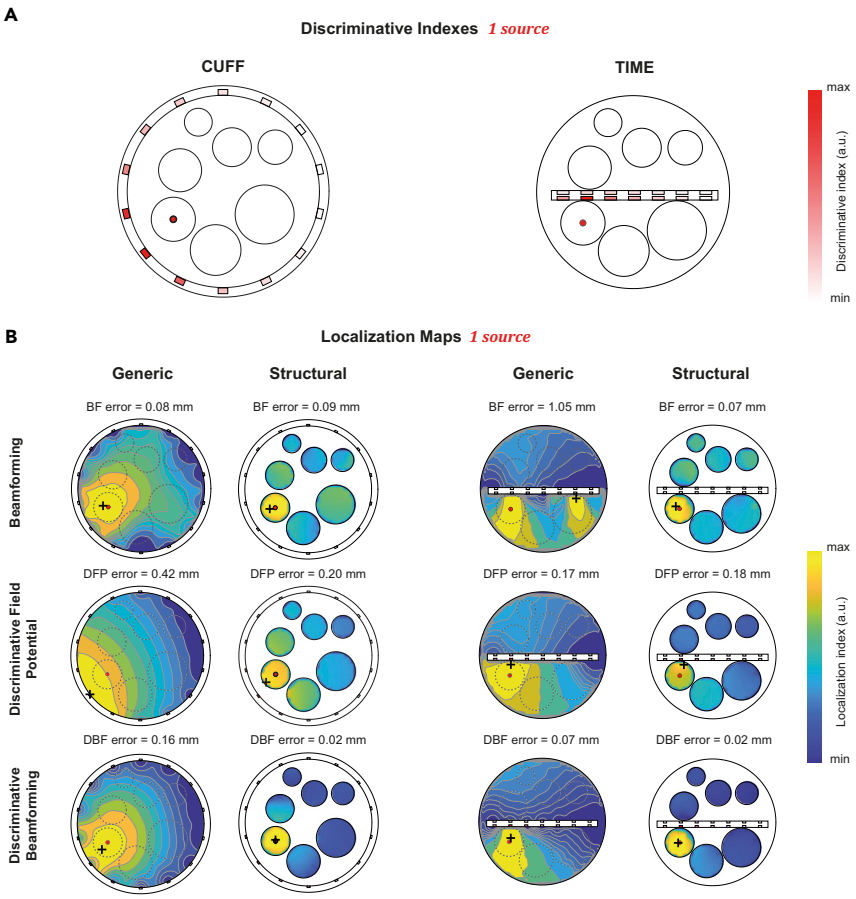

Figure 2. Single deterministic source discriminative indices and localization maps

(A) The discriminative index patterns of the cuff and TIME electrode for the selected ground truth map (red filled circles represent the spatial position of the source).

(B) Divided by electrodes, anatomical information available *a priori*, and methods. For the selected functional topography, the localization maps for each case are reported (black crosses represent the estimated spatial position of the sources).

distance between the predicted and the true locations of the target cluster of fibers. More details can be found in the experimental procedures.

DBF is more accurate for single-source localization

As a first experiment, the existing BF and DFP methods were compared with the new method, DBF, in localization of a single deterministic sinusoidal source oscillating at 4 Hz in Brownian noise. The discriminative index corresponding to each recording site was given by the power of the recorded signal in a narrow band around 4 Hz. We placed the single informative source inside each fascicle of each nerve topography, in turn performing a total of $N = 69$ simulations. For more details, see "single deterministic sinusoidal source in Brownian noise localization."

In Figure 2, illustrative simulation examples of estimated source localization maps by using the different source localization algorithms and discriminative index values for cuff and TIME electrodes are shown. We reported both cases where the information of a generic and structural model geometry is considered in the source localization algorithm pipeline. As we expected, independent of the considered electrodes, discriminative index values are higher for recording sites closer to the informative source and lower for sites that are farther away (Figure 2, top panels). When the generic model geometry is employed, it is evident that the BF-based methods (BF and DBF) produce more focal localizations, whereas DFP tends to identify a large area around recording sites (Figure 2, bottom panels). When a structural model is considered, accurate localization errors are obtained by all source localization algorithms (Figure 2, right column panels).

In Figure 3, localization error distributions for all performed simulations using BF, DFP, and DBF of the same case are shown. The distribution of random localization errors is also displayed. We found that our considered methods produced localizations maps that are significantly more precise than random localization ($p < 0.001$, $N = 96$, Kolmogorov-Smirnov test followed by Bonferroni correction for multiple comparisons.). The median, first, and third quartiles of the localization error distributions are shown in Table S1.

We employed a generalized linear (mixed-effects) model (GLM) to quantify and test the significance of the effect of the different localization algorithm, electrode, and geometrical model choices (the fixed effects in the model) and quantify the variability of the results because of different sections and fascicles (the random effects in the model). Because localization errors are positive definite, we assumed an underlying gamma distribution with link function $1/x$ so that positive values of fixed effect estimates indicate that they tend to decrease the localization error and vice versa. For more information, see experimental procedures "comparisons between source localization algorithms, electrode types, and geometrical models." We found that the DBF method improves significantly with respect to the BF, whereas the DFP does not lead to performance significantly different from BF (see Table 1, where the fixed effect estimates, standard errors, and p values are shown) The TIME leads to significantly worse localization estimates than a cuff electrode. Introducing structural information significantly improves performance (Table 1). Overall, the highest localization error decrease is provided by choosing the DBF method using cuff electrodes and incorporating a structural model geometry.

We found that random effect contributions are negligible with respect to the fixed effects, which means that there is not a strong systematic dependency of performance on the application of the localization methods for different nerve section topographies or different source fascicular locations (Table 1).

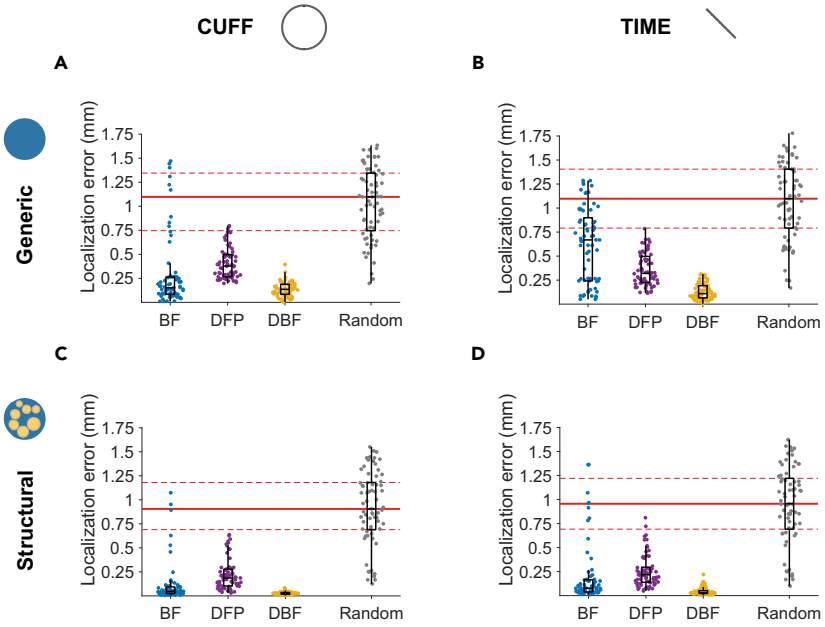

Figure 3. Single deterministic source localization

(A–D) Localization error distributions (N = 69) for (A) generic model and cuff electrode, (B) generic model and TIME, (C) structural model and cuff electrode, and (D) structural model and cuff electrode, divided by electrode (columns) and by anatomical information available *a priori* (rows). Outliers (1.5 IQR beyond the first or third quartiles) are depicted as isolated points outside of the boxplots. The dotted red lines correspond to the first and third quartiles of the distribution of localization errors for random localization, and the filled lines correspond to the median of the same distribution (experimental procedures). All distribution results are significantly different from the random (results).

Discriminative methods (DBF and DFP) are necessary for multiple-source localization

Next, we tested the ability of the three methods (BF, DFP, and DBF) to localize each one of three deterministic sinusoidal sources oscillating at 2 Hz, 4 Hz, and 16 Hz concurrently active in the nerve section. The discriminative index corresponding to each recording site and informative source was still computed as the power of the recorded ENG signals in a narrow band around the frequency of the target source, supposed to be known. We performed simulations varying nerve section topographies and choosing all possible assignments of the three informative sources to the different fascicles in each topography (N = 2119). For more information, see experimental procedures "multiple deterministic sinusoidal sources in brownian noise localization."

Table 1. Single deterministic source GLM parameter estimates

Fixed effects			
Name	Estimate	Standard error	P Value
(Intercept)	2.84	0.24	≪1e−5***
Electrode_TIME	−0.93	0.25	<1e−3***
Method_DFP	−0.0006	0.24	1.00
Method_DBF	8.02	0.69	≪1e−5***
Model_structural	3.15	0.33	≪1e−5***

Random effects	
Name	Standard deviation (Std)
Section	<1e−4
Fascicle | section	<1e−5

We report the estimate, standard error, and p value for the fixed effects on the localization errors given a gamma GLM with inverse link function. The reference level for electrode is CUFF, for method is BF, and for model is generic. Positive values correspond to decreasing the average localization error and negative values to increasing it. Higher values correspond to stronger effects. ***p < 0.001.

In Figure 4, we show an illustrative simulation example of typical discriminative index patterns for cuff and TIME electrodes and localization maps using BF, DFP, and DBF source localization methods. In the case of BF, the estimated localization maps tend to include all high-power regions as possible sources. For example, when using TIME electrode and generic model geometry, BF is completely misled by power sources that are closer to electrode sites and contribute maximally to the recorded signal power. In this specific case, DFP incorrectly localize sources in "shielded" fascicles, and we observed that the source is localized incorrectly in the fascicle between the electrode and the actual target fascicle. Instead, DBF provides an accurate estimate of the source position.

In Figure 5, localization error distributions for all performed simulations using BF, DFP, and DBF are shown. We found that our considered methods produced localization maps that are significantly more precise than random localization ($p < 0.001$, N = 2,119, Kolmogorov-Smirnov test followed by Bonferroni correction for multiple comparisons). However, BF produces a localization error distribution that, for a large part, falls in the interquartile range of random localization error distribution, discouraging its implementation. The median, first, and third quartiles of the localization error distributions are shown in Table S2.

A GLM was fit, as in the case of single-source localization, where we added a fixed effect linked to the frequency of the source to be localized. From the GLM fixed-effect estimates (see Table 2, where the fixed effect estimates, standard errors, and p values are reported), we found that the DFP and DBF methods improve significantly on the BF, whereas the DBF leads to a much more marked improvement. The TIME electrode leads to significantly worse localization estimates, and introducing structural information improves localization performance. To obtain an accurate functional map, the best choice is the DBF method, followed by a structural geometry model and a cuff electrode instead of a TIME.

We found that the random effect linked to the nerve section are negligible, whereas the location of the source to be localized in a given nerve section has a non-negligible effect on the localization error (Table 2). This means that, although localization error does

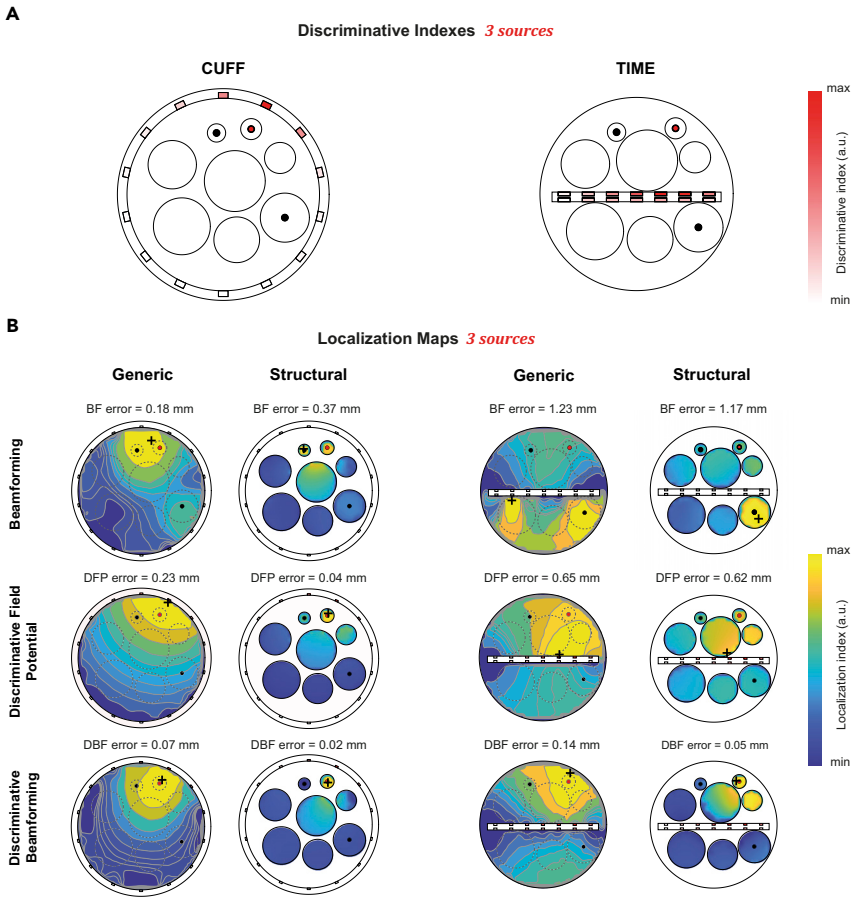

Figure 4. Multiple deterministic sources discriminative indices and localization maps

(A) For cuff and TIME electrodes, the discriminative index patterns for the considered source (red circle) in the selected ground truth map (red and black filled circles represent the spatial position of the sources).

(B) Divided by electrode, anatomical information available *a priori*, and methods. For the selected functional topography, the localization maps for each case are reported (black crosses represent the estimated spatial position of the red filled circle sources).

not vary substantially for different nerve sections, the location of the source in a given nerve section for a given recording electrode influences the precision of the localization result.

DBF precisely localizes multiple physiological functions in physiologically plausible recordings

Finally, we considered a biophysically realistic scenario by simulating physiologically plausible neural recordings via spiking fiber models (experimental procedures"generation of physiologically plausible neural recordings") and macroscopic physiologically variables, like blood pressure and respiratory signals, by using biophysically inspired dynamic system equations (experimental procedures"macroscopic physiological signal generation" and "supplemental experimental procedures"). Because the BF method performed poorly for multiple-source localizations, as shown in the previous section, here we considered only the DBF and DFP methods. We computed the discriminative indices as the ordinary least-squares estimates of the coefficients of a linear model expressing the ENG signal from each recording site, preprocessed according to the pipeline described under experimental procedures, as a linear combination of the two underlying physiological signals (blood pressure and respiration). We performed 96 simulations by varying nerve section topographies and sources fascicular locations (experimental procedures"multiple biophysical source localization").

In Figures 6A–6C and 7A–7C, vascular and respiratory physiological data generated at the different levels (i.e., macroscopic blood pressure and respiratory signals, nerve fiber spiking activity, and ENG recording sites) are shown. In the experimental procedures, the workflow for generation of simulated physiological and ENG signals is detailed. Signal-to-noise ratio (SNR) measures were consistent with real data experiments[19,20] (data not shown).

In Figures 6D and 7D, typical discriminative index patterns and localization maps for simulations performed using DFP and DBF in the case of blood pressure (BP) and respiration (RESP) source localization are shown, respectively. In all cases, the localization maps display the general features described in the previous sections; i.e., DFP tends to identify a large area around recording sites with respect to the DBF, and introducing a structural model improves localization performances.

Figure 8 shows localization error distributions for all performed simulations, using DFP and DBF of the same cases. We found that the DFP and DBF methods produced localization maps that were significantly more accurate than random localization ($p < 0.001$, $N = 96$, Kolmogorov-Smirnov test followed by Bonferroni correction for multiple comparisons). The median, first ,and third quartiles of the localization error distributions are shown in Table S3. Localization errors were also computed in terms of radial and angular components (Tables S5 and S6).

A GLM was fit, like in the previous experiments. With respect to the single deterministic source experiment, we added among the fixed effects the physiological function linked to each source. From the GLM fixed effect estimates, we can see that the DBF method produces a significantly more accurate localization than the DFP method (see Table 3 for fixed effect estimates, standard errors, and p values). Consistent with to previous sections' results, we found that choosing a DBF method using cuff electrodes and including structural information leads to optimal estimates of localization maps.

We found that the random effect linked to the nerve section is negligible with respect to fixed effects, whereas the location of the source to be localized in a given nerve section has a non-negligible effect on the localization error (Table 3).

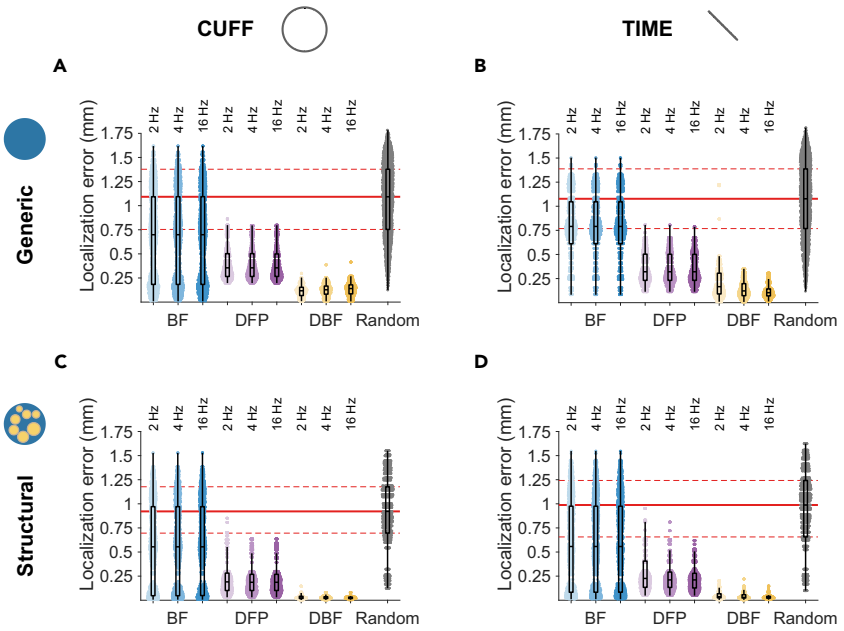

Figure 5. Multiple deterministic sources localization

(A–D) Localization error distributions (N = 2,118) for (A) generic model and cuff electrode, (B) generic model and TIME, (C) structural model and cuff electrode, and (D) structural model and TIME, divided by electrode (columns) and anatomical information available *a priori* (rows). Separate distributions are shown for each source concurrently active, according to their frequency (2 Hz, 4 Hz, and 16 Hz). Outliers (1.5 inter-quartile ranges [IQRs] beyond the first or third quartiles) are depicted as isolated points outside of the boxplots. The dotted red lines correspond to the first and third quartiles of the distribution of localization errors for random localization, and the filled lines correspond to the median of the same distribution (experimental procedures). All distribution results are significantly different from the random (results).

DBF and DFP are robust when considering reduced data size, electrode damage, and motion-related BP and RESP activity artifacts.

To understand how discriminative methods (DBF and DFP) are robust when considering possible constraints because of real experimental conditions, we tested the robustness of the DBF and DFP methods to available data size, electrode damage, and motion-related BP and RESP activity artifacts.

We estimated how much data are necessary for the DFP and DBF to give reliable localization functional maps. We studied different ENG signal durations from 0.1 s (4,000 samples) to 30 s (1,200,000 samples). In Figure 9, we report the simulation results, showing that discriminative methods are actually very robust in this data range size. We do not observe substantial degradation in the localization errors until 0.1-s duration (4,000 samples). We also found that performance increases with available data. To statistically test the robustness of the discriminative methods in case of reduced data points, we compared the localization errors under the 4,000 sample condition with the random localization error for all settings. We found significant differences between these two cases ($p < 0.001$, Kolmogorov-Smirnov test, N = 192, followed by Bonferroni correction for multiple comparisons). However, we can observe in Figure 9 that localization errors are not close to random values only for the case of a generic model and cuff electrodes (Figure 9A); thus, we discourage use of the other experimental setting with this available data size.

Electrode damage resulting in failure of active site recordings is an experimental phenomenon that affects the quality of ENG recordings. We thus investigated the effect on localization error of not considering a number of recording sites because of electrode damage (experimental procedures"source localization algorithms"). We performed simulations with 1, 2, 5, 10, and 12 damaged recording sites. The results of the simulations are reported in Figure 10, showing that localization errors increase with the number of broken channels (as expected) for all possible experimental settings. We found that, up to approximately one third of damaged electrodes (i.e., 5 broken channels of 14), the localization error curves are flat, indicating robustness of the algorithms. We tested the robustness of the methods in the case of highly damage electrodes by comparing the localization errors for the case of 12 broken channels with the random localization error, and we found a significant difference between these two cases ($p < 0.001$, Kolmogorov-Smirnov test, N = 192, BP and RESP concatenated). These results indicate that, in principle, even when more than two thirds of the electrodes are unusable (i.e., 12 broken channels of 14), our algorithm is significantly better than random localization, but we can see in Figure 10 that localization errors are close to random values; thus, we discourage use of a highly broken electrode for functional localization purposes.

We studied the robustness of discriminative methods (DBF and DFP) in the presence of motion-related BP and RESP activity

Table 2. Multiple deterministic sources GLM parameter estimates

Fixed effects			
Name	Estimate	Standard error	p value
(Intercept)	1.43	0.08	≪1e−5***
Electrode_TIME	−0.16	0.01	≪1e−5***
Method_DFP	1.56	0.02	≪1e−5***
Method_DBF	9.17	0.06	≪1e−5***
Model_structural	0.77	0.02	≪1e−5***
Frequency	0.005	0.001	<1e−3***
Random effects			
Name			Std
Section			<1e−4
Fascicle | section			0.63

We report the estimate, standard error, and p value for the fixed effects on the localization errors given a gamma GLM with inverse link function. The reference level for electrode is CUFF, for method is BF, and for model is generic. Positive values correspond to decreasing the average localization error and negative values to increasing it. Higher values correspond to stronger effects. ***$p < 0.001$.

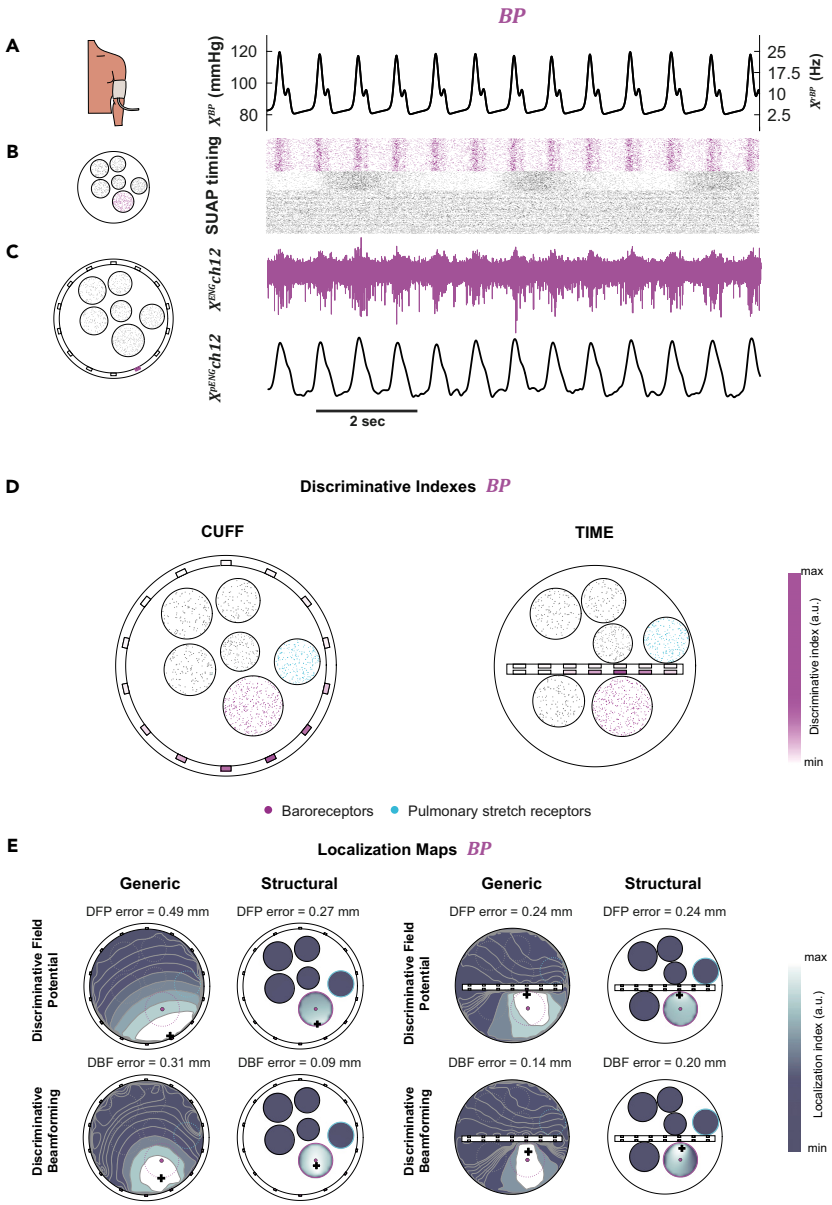

Figure 6. BP discriminative indices and localization maps

(A) The simulated BP signal used to generate the ENG signals and compute the discriminative indices.

(B) The raster plots show plausible firing patterns, highlighting in plum purple the activity of the baroreceptors.

(C) The simulated ENG recordings, plotting the signals recorded by the channel in purple; i.e., the closest active site to the fascicle containing the baroreceptors. The same signal was pre-processed and plotted below.

(D) The discriminative index patterns of the cuff and TIME electrode for the selected maps is shown graphically, referring to the legend on the right.

(E) Divided by electrode, by anatomical information available *a priori*, and methods. For the selected functional topography (purple filled circles represent the center of the spatial position of the sources), the localization maps for each case are reported, referring to the legend on the bottom right.

artifacts (experimental procedures"multiple biophysical source localization"). We considered the case of cuff electrodes; in Figures 11A and 11B, a representative set of simulated ENG recordings affected by spurious physiological signal modulation with different effects with respect to channel position are shown. In Figure 11E, localization error distributions for each method are shown. We compared the discriminative methods' performance with the random localization error by a Kolmogorov-Smirnov test on the three distributions versus random (N = 192, BP and RESP concatenated), followed by Bonferroni correction for multiple comparisons. We found that all methods perform significantly better than random ($p < 0.001$). We also tested the differences among the performance of the two methods, DFP versus DBF, and we found that DFP performs significantly better than DBF ($p < 0.001$, Kolmogorov-Smirnov test, N = 192, BP and RESP concatenated). Finally, we assessed the differences in the DBF and DFP methods in cases with and without noise effect, and we found that, for BP and RESP localization, noise effect significantly affects the performance of the two methods ($p < 0.001$, Kolmogorov-Smirnov test, N = 96). DBF and DFP are sensible with respect to multiplicative noise effect but still provide good localization errors significantly better than random guessing. DBF turned out to be the best method for functional localization, even in the presence of multiplicative noise.

DISCUSSION

The efficacy of VN bioelectronic neuromodulation strongly depends on spatially selective neuromodulation protocols based on VN functional topography. Here we proposed a method to spatially localize simultaneous cardiorespiratory functions within the VN by exploiting ENG signals recorded during spontaneous neural activity. Our new method, called DBF, was developed by combining two existing approaches: the BF method,[12] providing a spatial map of neural fiber activity in terms of their power, and discriminative indices of neural interfaces, characterizing the ability of recording sites to assess relevant functional information.[15]

We tested our method on a realistic nerve model geometry of the human cervical VN implanted via epineural (cuff) or intraneural (TIME) electrodes. We outlined a way to incorporate structural information in the localization algorithm by forcing the output of source localizations only inside fascicles. We considered three different ground truth scenarios of multi-functional topography generated by single- and multiple-frequency sinusoidal neural fiber activities immersed in Brownian background noise and a biophysically realistic model of cardiorespiratory neural fiber activities.

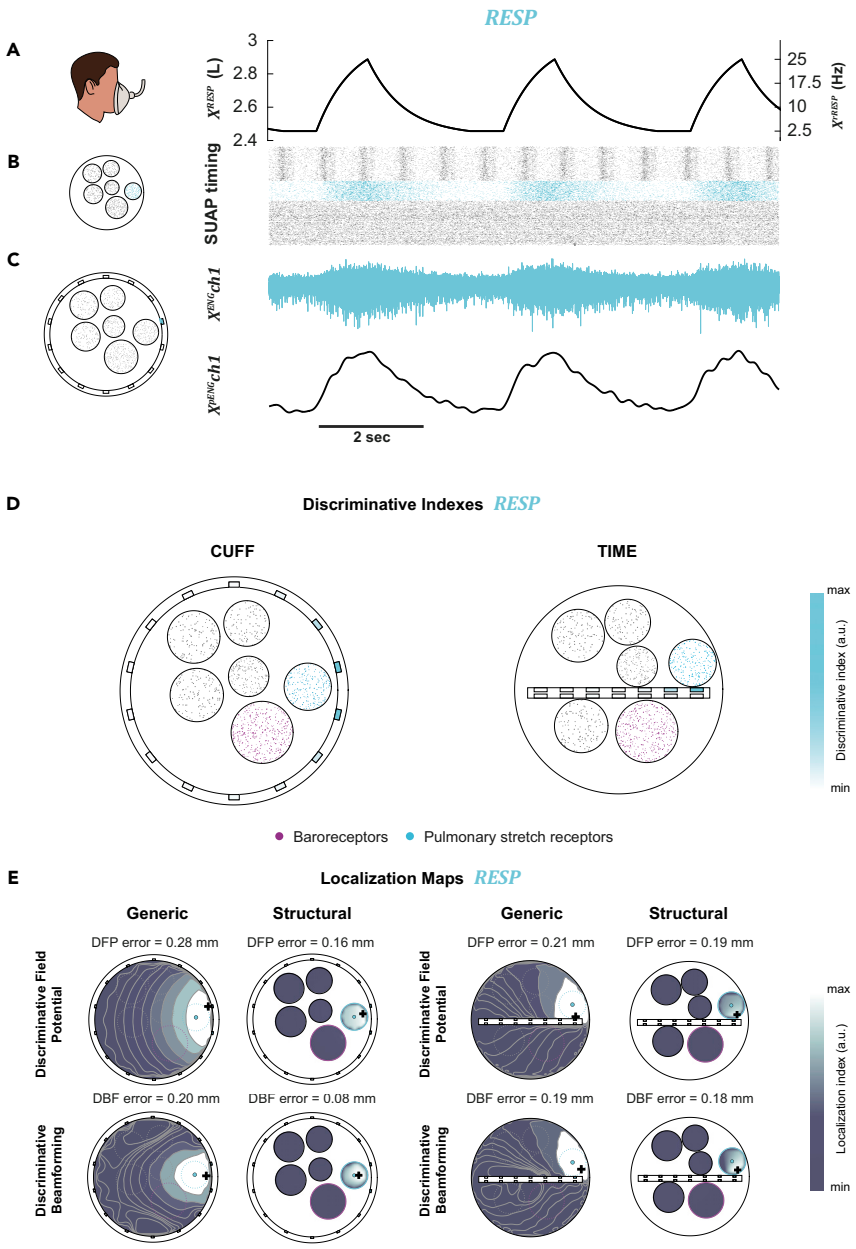

Figure 7. RESP discriminative indices and localization maps

(A) The simulated RESP signal used to generate the ENG signals and compute the discriminative indices.

(B) The raster plots show plausible firing patterns, highlighting in light blue the activity of the pulmonary stretch receptors.

(C) The simulated ENG recordings, plotting the signals recorded by the channel in light blue; i.e., the closest active site to the fascicle containing the pulmonary stretch receptors. The same signal was pre-processed and plotted below.

(D) The discriminative index patterns of the cuff and TIME electrode for the selected maps is shown graphically, referring to the legend on the right.

(E) Divided by electrode, anatomical information available *a priori*, and methods. For the selected functional topography (light blue filled circles represent the center of the spatial position of the sources), the localization maps for each case are reported, referring to the legend on the bottom right.

Under all tested conditions, the DBF method provides accurate estimates of the underlying multi-functional topographical organization, outperforming previous methods like BF[12] and DFP[15] (Figures 3, 5, and 8; Tables 1, 2, and 3). In all settings and for all methods, adding structural information significantly improved localization predictions (Tables 1, 2, and 3), justifying efforts to obtain *in vivo* structural information. We found that discriminative methods are quite robust when considering possible experimental constraints, such as reduced data size, electrode damage, and motion-related BP and RESP activity artifacts (Figures 9, 10, and 11). DBF in particular turned out to be the best method for functional localization, even in the presence of multiplicative noise related to BP and RESP activity artifacts.

In the case of single-source localization, DBF outperformed BF. This can be justified by noticing that DBF employs the recorded signal power in a narrow band around the informative source frequency, whereas BF employs the total power of the of the ENG signals. Both capture the whole informative source power, but in the DBF, the noise contribution is integrated only in a small band, providing more accurate localizations.

We found that the BF method performs poorly in the case of multiple sources by providing a localization error distribution that falls for a large part in the interquartile range of random localization error distribution (Figure 5). Although BF generally produces multimodal localization maps, where the modes correspond to all different power hotspots present in the nerve (noisy or informative; see Figure 4 for sample localization maps for multiple sources concurrently active in the nerve), it is unable to refer each of these hotspots to the different functions because its definition does not include any "discriminative" measure. Very frequently, the estimated source position was the location of the hotspot at a minimum distance from a recording site so that its power has a larger contribution to the recorded ENG power. The fact that BF is not intrinsically "discriminative" requires inducing a higher activation in the fiber cluster being localized so that its contribution to the recorded ENG total power is higher, as was done previously.[12]

We observed that DBF provides more focal results with respect to DFP (Figures 2, 4, 6, and 7). We expected this result because, in the inversion of the LFM, the column corresponding to the field of view of each recording site is adjusted, taking into account the field of view of the other recording sites as well. On

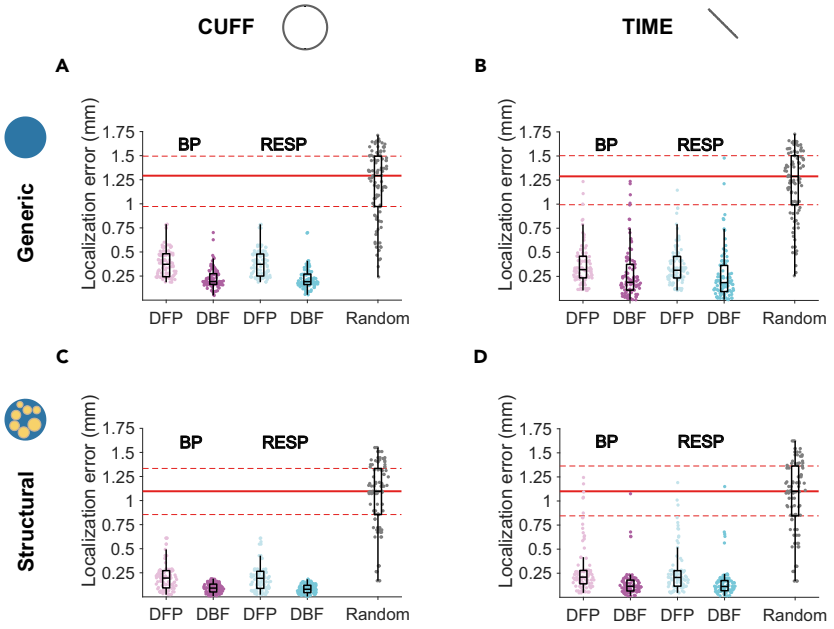

Figure 8. Multiple biophysical source localization

(A–D) Localization error distributions (N = 96) for (A) generic model and cuff electrode, (B) generic model and TIME, (C) structural model and cuff electrode, and (D) structural model and cuff electrode, divided by electrode (columns) and anatomical information available *a priori* (rows). Separate distributions are shown for each source concurrently active, according to their function (BP or RESP). Outliers (1.5 IQR beyond the first or third quartiles) are depicted as isolated points outside of the boxplots. The dotted red lines correspond to the first and third quartiles of the distribution of localization errors for random localization, and the filled lines correspond to the median of the same distribution (experimental procedures). All distribution results are significantly different from the random (results).

the contrary, DFP directly used the LFM without any such adjustment, leading to broad localization patterns with maxima often in correspondence with electrode sites (where the LFM entries are highest). In the structural case, the DFP method can be fooled by shielding fascicles (Figure 4, TIME electrode cases). The source is localized in the very large fascicle, covering the true location of the informative source, because DFP tends to put out localization positions close to electrode sites. DBF solves this problem employing the inverse LFM, exploiting the correlation between recordings from the different sites.

To determine the optimal peripheral interface to perform multifunctional localization maps, we tested epineural cuff electrodes and intraneural TIME interfaces. We found that cuff electrodes allow better localization maps with respect to TIME. We justified these results because cuff electrodes are characterized by a truly bi-dimensional structure more suitable for bi-dimensional nerve section, while employing the one-dimensional TIME leads in general to worse but still acceptable performance.

Table 3. Multiple biophysical source GLM parameter estimates

Fixed effects			
Name	Estimate	SE	p Value
(Intercept)	3.20	0.25	≪1e−5***
Electrode_TIME	−0.52	0.13	<1e−3***
Method_DBF	1.96	0.15	≪1e−5***
Model_structural	1.97	0.15	≪1e−5***
Function_RESP	0.07	0.12	0.59
Random effects			
Name		Std	
Section		<1e−3	
Fascicle | section		1.22	

We report the estimate, standard error, and p value for the fixed effects on the localization errors given a gamma GLM with inverse link function. The reference level for electrode is CUFF, for method DFP, and for model is generic. Positive values correspond to decreasing the average localization error and negative values to increasing it. Higher values correspond to stronger effects. ***p < 0.001.

Overall, the *in silico* experiments suggest that the lowest localization errors for multiple function localization in the VN can be obtained by employing DBF using ENG recordings from a cuff electrode implanted on a nerve whose structure is known. However, when moving to humans, obtaining *in vivo* structural information may not be feasible, inaccurate, or available only for the part of the exposed nerve facing the surgical access. For these reasons, in clinical settings, a realistic combination of the proposed methods could be use of a generic model of the nerve and cuff electrodes for ENG recordings.

Our discriminative methods are strongly related to the work of Ravagli et al.[16] and Thompson et al.,[17] who include experimental testing of a technique (EIT) for locating neural activity sources across the cross-section of the VN using auxiliary information from RESP/heartbeat signals. EIT can be seen as a DBF algorithm where the discriminative coefficients are computed using the correlation between the measured spontaneous impedance variation and a physiological signal. Measurement of such impedance variation requires injection of a low-amplitude, high-frequency current that does not alter physiological functions but still requires a specific experimental setup, and it takes quite a long time to perform measurements from different stimulation sites. Our discriminative algorithm employs only the recorded ENG signal, which highly simplifies the setup, experimental protocol, and low computational time (∼13 and 25 s for DFP and DBF, respectively; calculated for simulations in biophysical source experiments). Although the theoretical time and space resolution of EIT is extremely good, we believe that a true comparison of the typical errors of EIT and discriminative methods would require performing both under the same experimental conditions for future development of peripheral nerve functional topography characterization.

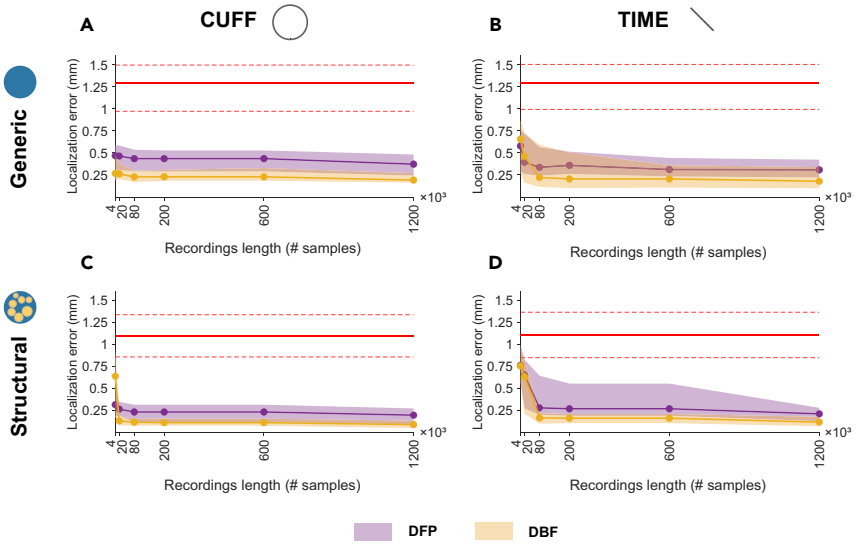

Figure 9. Source localization with reduced data samples

(A–D) Quartile (Q1–Q3) area plots about the localization error distributions (N = 96) for (A) generic model and cuff electrode, (B) generic model and TIME, (C) structural model and cuff electrode, and (D) structural model and cuff electrode, divided by electrode (columns) and by anatomical information available *a priori* (rows). Separate areas are shown for DFP and DBF, represented in purple and orange, respectively. The filled lines correspond to the median of the same distribution (experimental procedures). The worst-case distribution on each axis, corresponding to 4,000 samples, shows results significantly different from the random (results).

Limitations and future directions

An important step for the reliability of our source localization method is the choice of discriminative index. The definition of a discriminative index requires *a priori* knowledge of the relation between neural fiber activity and macroscopic physiological variables like BP and RESP signals. In our work, based on previous studies on VN recordings in anesthetized pigs[19,20] and VN microneurographic recordings in healthy humans,[21] we assumed a linear relationship between cardiorespiratory variables (i.e., BP and RESP) and the related fiber firing rates. However, in non-anesthetized and/or pathological situations, the simple linear relationships between neural activity patterns and macroscopic physiological variables can be altered, leading to incorrect predictions. To overcome this limitation, different discriminative indices based on more complex non-linear relations can be concurrently employed and compared with the linear case. In our model, we did not consider the possible delay between measurable physiological signals and the underlying neural activity. Although the computation of the discriminative indices is most likely not robust with respect to such delay, this problem can be solved by simply shifting one of the two signals on the other until the discriminative indices are maximized. If different functions are linked to the corresponding neural activity via different delays, then more complex linear models, like autoregressive moving-average (ARMA) models, which incorporate delays, should be employed to compute the discriminative indices.

Here we tested our method by using synthetic signals and known ground truth functional spatial maps. The presented method should be validated in real experimental settings where the functional spatial map is unknown. To this aim, we could perform animal model experiments by combining ENG recordings during spontaneous activity and altered physiological states, stimulation protocols assessing the functional role of a specific spatial region of the VN, and structural information to build animal-specific structural-functional maps. Similar to Vallone et al.,[15] we could record electroneurographic signals from pig VN corresponding to baseline conditions (i.e., spontaneous activity) and altered physiological states, like increasing BP values and RESP rate. This protocol could provide the means to compare localization maps during spontaneous activity and altered physiological states. We would be able to test our localization methods by observing a substantial spatial overlap between the inferred spatial maps for a given physiological function during baseline activity and the corresponding altered state for the given function. In a similar manner, recent stimulation protocols to test organ- and function-specific organization of the pig VN[11] could also be applied to test the efficiency of our localization method by comparing spontaneous localization maps and electrically induced functional maps for a given physiological function. Finally, structural information could also be employed by following a procedure developed previously[22] to visualize the fascicular organization of the pig VN *in vivo* and build animal-specific structural-functional maps.

Regarding the choice of selective stimulation parameters, when the localization map for a given function has been obtained, we could assume that the corresponding fiber group is located in the fascicle that is closest to the maximum of the localization map or in the fascicle that has the largest intersection with a given level set of the localization map. Then we can determine the selectivity of the stimulation of such fascicles according to several single- or multi-site stimulation protocols using hybrid modeling.[23] To estimate target and off-target recruitment at a low computational cost and cover a large enough subset of the possible stimulation protocols in a reasonable amount of time, model-based methods like activating function formalism can be employed, similar to what has been presented previously.[24]

Conclusions

We developed a method for spatially mapping simultaneous multi-functional VN activity from ENG signals recorded during spontaneous activity. We tested our method over three different ground truth scenarios generated via *in silico* experiments, considering a realistic geometry of the human VN and an increasing complexity of simultaneous multi-functional neural activity.

Our method reliably provides an accurate estimation of the multi-functional VN topography under all tested ground truth scenarios. Our method significantly outperforms two previous approaches, allowing generation of a precise multi-functional topographical map for an implanted human VN.

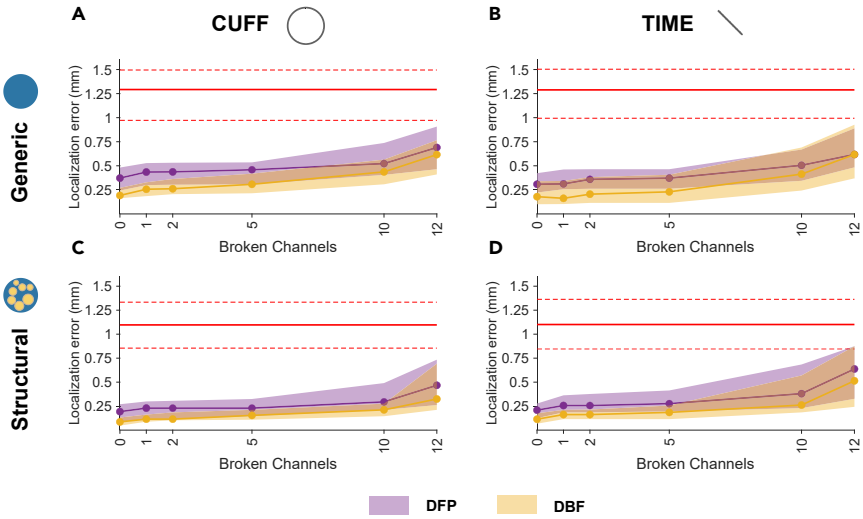

Figure 10. Source localization with reduced numbers of working channels

(A–D) Q1–Q3 area plots about the localization error distributions (N = 96) for (A) generic model and cuff electrode, (B) generic model and TIME, (C) structural model and cuff electrode, and (D) structural model and cuff electrode, divided by electrode (columns) and anatomical information available *a priori* (rows). Separate areas are shown for DFP and DBF, represented in purple and orange, respectively. The filled lines correspond to the median of the same distribution (experimental procedures). The worst-case distribution on each axis, corresponding to 12 broken channels, shows results significantly different from the random (results).

We developed a methodological framework for *in vivo* functional imaging of peripheral nerves through electro-neurographic recordings acquired during spontaneous activity, reducing the invasiveness of stimulation protocols and related side effects.

The present study could pave the way for development of spatially selective stimulation protocols targeting multiple bodily functions at the same time via a single neural interface.

EXPERIMENTAL PROCEDURES

Resource availability

Lead contact

The lead contact for this work is S.M. (silvestro.micera@epfl.ch).

Materials availability

This study did not generate new unique reagents.

Data and code availability

All data and code needed to replicate the results of the present work are publicly available at https://github.com/s-romeni/vagus_nerve_discriminative_beamforming.

Nerve 3D model geometry

Ten hypersimplified nerve morphologies (circular fascicles in a circular nerve[23]) were produced, following the typical statistics of the left cervical human VN[9] (Figure S1). The diameter of the nerve was set to 2 mm, and the number of fascicles was sampled from a uniform distribution defined in the interval [6, 8] and for their diameter in [0.15, 0.7] mm. The fascicles were packed using the *a priori* check for intersections (ACI) packing algorithm presented previously[23] (Figure 1A).

The thickness of the perineurial sheath was set to 0.03 times the diameter, according to Grinberg et al.[25] The cross-sectional morphologies were extruded for 20 mm to obtain 3D nerve segments, and a cuff electrode or a TIME[18] were added to the geometry. The TIME was modeled as in Romeni et al.[23] (14 active sites), and the cuff is composed of a hollow cylinder (the "shaft") and 14 small cylindrical conductive sites (the recording sites) equispaced along the circumference of the internal surface of the shaft so that their "internal" surface was fully in contact with the nerve epineurium. In both electrode types, a height of 30 μm and a radius of 25 μm were used for the size of the active sites. When a TIME was added, fascicles were automatically displaced so that no recording site was in any fascicle (Figure 1B).

In Figure 1C, we show how each nerve section is divided into different solid domains modeled as homogeneous (possibly anisotropic) conductive medium with electrical properties taken from Romeni et al.[23] Following an approach adopted previously,[12] two models with different structure complexity were used in this work. We call the ensemble of the obtained 3D nerve segment with the implanted electrode the "structural model" of the nerve and a derived model obtained by removing all fascicular components (perineurium, endoneurium) the "generic model" of the nerve (Figure 1D).

Reciprocity theorem and LFM

We used the structural model to compute the signal recorded at the electrode sites, which was used to determine function localization. We assumed (as is customary; see, for example, Wodlinger and Durand[12] and Jehenne et al.[26]) that the modeled media were linear and quasi-static.[27] We collected, in a matrix L_{ij}, the so-called LFM of our problem, the values of the potential at a recording site j because of a unitary membrane current at a fiber node i, computed through FEM. If the membrane current at a fiber node i is $\iota_i(t)$, then its contribution at recording site j will be $v_{ij}(t) = \cdot\iota_i(t)L_{ij}$. Using the superposition principle, the recorded potential at site j (Figure 2C) because of the joint action of all active fiber nodes is simply

$$v_j(t) = \sum_i v_{ij}(t) = \sum_i \iota_i(t)L_{ij}.$$

To reduce the computational load of calculating the LFM, it is customary to employ the so called "reciprocity theorem." The theorem states that, in a purely resistive medium, the electric potential at point j because of a current injected at point i is equal to the electric potential at point i because of the same current applied in j. Thus, we can compute the potential recorded at a given electrode site because of a current injected at a given fiber node by determining the potential at that fiber node because of a current injected at the recording site. This hugely reduces the computational load of our problem because it requires a number of FEM runs equal to the number of recording sites, which is much lower than the number of fiber nodes (Figure 1E).

Source localization algorithms

As we already anticipated, the signal recorded by an electrode site can be seen as a linear combination of the neural sources, weighted by the LFM entries corresponding to the specific fiber node locations. When we perform source localization, we do not know in general the location of each neural source and, thus, cannot employ the LFM that "generates the recorded signals."

Here we discretize the nerve section into a $M \times M$ square grid and suppose that each cell grid (called pixel hereafter) is a potential neural source. We indicate the LFM employed in the localization as $\widehat{L} \in \mathbb{R}^{P \times R}$, where $P = M^2$ is the number of pixels in the nerve section, and R is the number of recording sites. The "theoretical" LFM, employed in generation of neural signals from nodal current, will be instead indicated as above with $L \in \mathbb{R}^{S \times R}$, where S is the number of actual neural sources. Because we assumed that all recording sites were located on a plane transverse to the nerve path, here we considered only the reconstruction of the sources in a section of the nerve.

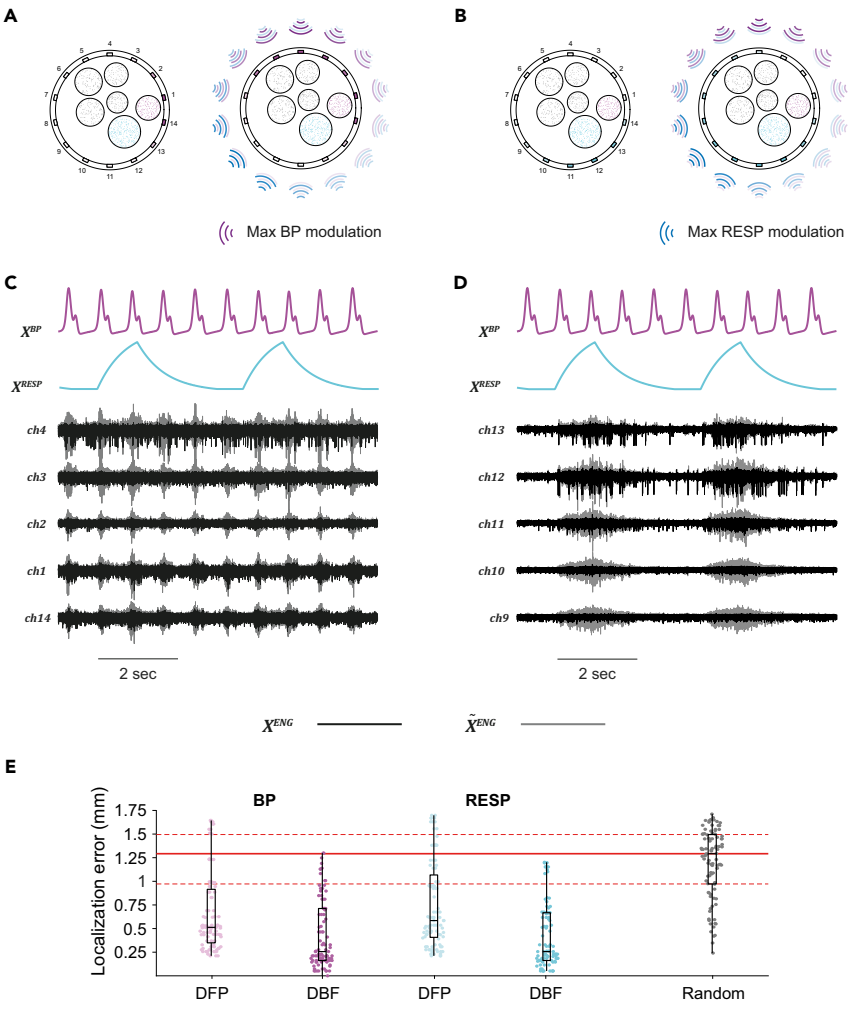

Figure 11. Source localization with correlated noise artifacts

(A and B) Discriminative indices without and with the multiplicative noise effect, respectively, for the BP and the RESP localization. It highlights the spatial proportionality of the interference (experimental procedures), using the purple and blue waves outside of the section, as shown by the legend.

(C and D) The physiological signals and neural recordings of the channel more affected by the noise without (black) and with (gray) the multiplicative noise effect, respectively, for the BP and the RESP localization.

(E) the localization error distributions (N = 96) for the generic model with a cuff electrode. Separate distributions are shown for each source concurrently active, according to their function (BP or RESP). Outliers (1.5 IQR beyond the first or third quartiles) are depicted as isolated points outside of the boxplots. The dotted red lines correspond to the first and third quartiles of the distribution of localization errors for random localization, and the filled lines correspond to the median of the same distribution (experimental procedures). All distribution results are significantly different from the random (results).

Depending on the *a priori* information available about the nerve fascicular topography, the localization LFM can be built using the structural or the generic model geometry. To incorporate *a priori* information, we proceeded similar to Babiloni et al.[28] by computing a weighted pseudo-inverse LFM

$$\widehat{L}_{\Lambda}^{+} = \left(\widehat{L}^{T}\Lambda\widehat{L}\right)^{-1}\widehat{L}^{T}\Lambda \in \mathbb{R}^{R\times P},$$

where $\Lambda \in \mathbb{R}^{P\times P}$ is a diagonal matrix whose i-th entry is 1 when the corresponding pixel location can contain a source or 0 when it cannot. For example, all pixels that fall outside of the external boundary of the nerve or in the TIME shaft are assigned a 0 weight because no neural source can be there. In the case of $\widehat{L}$ being the structural LFM, all pixels outside of fascicles are given a 0 weight.

Following Wodlinger and Durand,[12] we channel-wise normalized the pseudo-inverse LFM to reduce the probability to have a solution with pixels close to the recording site while increasing the probability to find the solution even far from the recording site; i.e.,

$$\widehat{L}_{\Lambda}^{+}[:,j] \leftarrow \frac{\widehat{L}_{\Lambda}^{+}[:,j]}{\Lambda\widehat{L}\widehat{L}_{\Lambda}^{+}[:,j]_2},$$

where $||\cdot||_2$ indicates the L2 norm (hereafter we drop the Λ subscript to avoid overly complicated notation).

In the BF,[12] the localization map was computed as

$$\varphi_{p}^{BF} = \sum_{r} P_r \cdot [\widehat{L}^{+}]_{r,p},$$

where P_r is the total power (computed as the root mean square) of the signal recorded by recording site r.

We previously[15] introduced the idea of a discriminative index characterizing the ability of the different recording sites to acquire relevant information about a physiological activity cluster. For example, previously,[15] the discriminative index $D_{c,r}$ for the activity cluster c and the recording site r was a measure of the ability of the recording site to provide information to deduce when activity cluster c was modulated (Figure 1F). The discriminative index induces an importance ordering of the recording sites and can be used to weight the "fields of view" of each recording site in a "localization map" (Figure 1G). These considerations helped to define a localization index, the DFP, as

$$\varphi_{p,c}^{DFP} = \frac{\sum_r [\widehat{L}]_{p,r} D_{r,c}}{\sum_r [\widehat{L}]_{p,r}},$$

where $D_{r,c}$ is the discriminability coefficient corresponding to recording site r and physiological activity cluster c.

DBF used the localization map

$$\varphi_{c,p}^{DBF} = \sum_{r} D_{c,r}[\widehat{L}^{+}]_{r,p}.$$

We can see that BF is a subcase of DBF, where $D_{c,r}$ was set equal to the r-th channel power for all activity clusters. For this reason, BF can at most detected activity clusters but cannot discriminated them. DBF can be thought of as operating "cluster-wise filtering," because it enhances the components of the inverse LFM that can better capture relevant information from the source of interest.

With all source localization methods, the estimated source position was equal to the spatial position corresponding to the maximum value of the considered localization map. The localization error was estimated by computing the Euclidean distance between the original position and the estimated one (Figure 1H). When electrode damage was studied, we first excluded the signals corresponding to the damaged recording channels in

the calculation of the discrimination indices, and then it was necessary to redefine the lead-field matrix as $\widehat{L} \in \mathbb{R}^{P\times A}$, where $P = M^2$ is the number of pixels in the nerve section, and A is the number of available recording sites before calculation of the localization methods.

To spatially visualize the results in the nerve section, on the localization map matrix with an original dimension of 40 × 40 pixels (a single pixel corresponds to 50 μm), we first applied a spatial resampling, generating 1,000 × 1,000 pixels, and then we applied a smoothing spatial filtering (moving average on a 30 × 30 pixels square kernel), obtaining a smoothed localization map matrix. In the generic model geometry, we draw a contour plot with 10 isolines increasing every 10 percentiles of the smoothed localization map matrix, whereas for the structural model geometry, we plotted the values of the smoothed localization map matrix. To distinguish those values from the original localization map, we called this the new quantity localization index (Figure 1H).

In silico experiments and discriminative index definitions

Single deterministic sinusoidal source in Brownian noise localization

As a first *in silico* experiment, we tried to localize a single informative source immersed in a Brownian ($1/f^2$) background noise. Specifically, we located a sinusoidal source with a frequency $f_0 = 4$ Hz and amplitude of 1 μA in the most central pixel of a selected fascicle and noise sources in the remaining pixels of the fascicles. Five minutes of sinusoidal signal was generated using a sampling frequency of 100 Hz. We generated Brownian noise time series using the MATLAB function dsp.ColoredNoise, and then we scaled them so that the average SNR across recording sites had value 1. Specifically, let us indicate the array of informative signals as

$$S(t) = [0, \ldots 0, \boldsymbol{s}(t), 0, \ldots, 0] \in \mathbb{R}^{P\times T},$$

where $\mathbf{s}(t)$ is a time series of duration equal to T so that recording site r records the informative signal

$$S_r(t) = \widehat{L}_r S(t),$$

where $\widehat{L}_r \in \mathbb{R}^{1\times P}$.

Let us also indicate the noise time series obtained through MATLAB as $[R_1(t), \ldots, 0, \ldots, R_n(t)]$, where 0 is in the location corresponding to the informative source. These noise signals are scaled with a constant α so that the noise signal is

$$R(t;\alpha) = [\alpha \boldsymbol{R}_1(t), \ldots, 0, \ldots, \alpha \boldsymbol{R}_n(t)] \in \mathbb{R}^{P\times T}$$

and the contribution of the noise signal to the r-th site recording is

$$R_r = \widehat{L}_r R.$$

We fixed the parameter α so that

$$SNR = \frac{1}{N_r}\sum_r \frac{P[S_r(t)]}{P[R_r(t;\alpha)]} = 1.$$

We computed the discrimination coefficient for a given recording site as the power of the signal recorded by the given site in a band with a half-width $\delta f = 0.1$ Hz around the sinusoid frequency $f_0 = 4$ Hz .

$$D_{f_0,r} = P(S_r(t), [f_0 - \delta f, f_0 + \delta f])$$

In this way, recording sites closest to the informative source have a higher discriminative coefficient value because the contribution of the informative source is higher, whereas the contribution of the noisy background is comparable at all sites. We performed one set of simulations for each electrode (TIME and cuff), model of the nerve (generic and structural), and nerve fascicular topography (10 topographies; Figure S1), placing the source, in turn, in each fascicle of the section. For each set of simulations, we placed the single informative source in the center of each fascicle in turn, obtaining a number of simulations equal to the number of fascicles in all nerve topographies.

Multiple deterministic sinusoidal sources in Brownian noise localization

As a second *in silico* experiment, we considered the localization of concurrently active informative sources. Background noise was obtained by locating Brownian noise sources in all pixels free of informative sources. The same scaling factor α was employed for noise time series so that the SNR for each source is indeed lower than 1 because of the presence of the other informative sources, which have the same amplitude.

We considered the case of three sinusoidal sources with frequencies equal to 2 Hz, 4 Hz, and 16 Hz. The employed discrimination coefficient was the same as in the case of single source localization, namely

$$D_{f_i,r} = P\left(S_r^{(i)}(t), [f_i - \delta f, f_i + \delta f]\right),$$

with $S_r^{(i)}$ being the contribution to the recording from site r of the signal from informative source i, and $f_i = \{2, 4, 16\}$ Hz.

We performed one set of simulations for each electrode (TIME and cuff), model of the nerve (generic and structural), and nerve fascicular topography (10 topographies; Figure S1) by testing all partial permutations of the three sources for any choice of three fascicles in a given section, which correspond to a number of simulations equal to $N_{fasc}!/(N_{fasc} - N_{sources})!$.

Multiple biophysical source localization

We tested the capabilities of our algorithms in a more realistic setting where signals from informative sources were generated through biophysical modeling. Specifically, we simulated neural fiber activity generating ENG signals, X^{ENG}, and two macroscopic physiological signals, X^{BP} and X^{RESP}, which represent the BP and RESP signals during spontaneous activity, respectively (see "macroscopic physiological signal generation" for details).

The simulated ENG signals are processed using the following pipeline: band-pass filtering ([1,000, 6,000] Hz, elliptic filter, fourth order), squaring, moving average (150-ms window), square root extraction, low-pass filtering (Butterworth filters, fourth order, with a cutoff frequency of 10 Hz and 4 Hz corresponding to *BP*- and *RESP*-related source localization).

The discriminability coefficients, for a specific recording site r and macroscopic physiological signal $c = \{BP, RESP\}$, are defined here as the coefficients for the regressors $D_{c,r}$ in the linear problem

$$X_{t,r}^{pENG} = X_{t,c}^{physio} D_{c,r} + \varepsilon_{t,r},$$

where X^{pENG} is the processed ENG signal matrix; $X_c^{physio} = [X^{BP}, X^{RESP}]$ represents the BP and RESP signals, respectively; and $\varepsilon_{t,r}$ is a zero mean, unknown variance Gaussian noise.

The discriminability coefficients are computed using the ordinary least squares estimator

$$D = \left(X^{physio}\right)^{+} X^{ENG},$$

where we indicate with the subscript (+) the Moore-Penrose pseudo-inverse matrix.

We performed one set of simulations for each electrode (TIME and cuff), model of the nerve (generic and structural), and nerve fascicular topography (10 topographies; Figure S1) by testing all partial permutations of the two physiological sources for any set of two afferent fascicles in a given section, which correspond to a number of simulations equal to $(N_{fasc} - \text{floor}(N_{fasc}/2))!/((N_{fasc} - \text{floor}(N_{fasc}/2)) - N_{sources})!$.

Multiple biophysical source localization in the presence of motion-related BP and RESP activity artifacts

Motion-related BP and RESP activity artifacts are present in real data experiment affecting the quality of the recordings. For this reason, we tested the robustness of the source localization algorithms in the presence of these motion-related artifacts. considering an additional ENG model signals containing a BP- and RESP-correlated multiplicative noise causing a time-varying contact impedance with location dependence.

The additional ENG model, including multiplicative noise, reads

$$\tilde{X}_r^{ENG} = X_r^{ENG}(t) \cdot \left(1 + \beta_{RESP,r} \cdot g_{RESP}(t) + \beta_{BP,r} \cdot g_{BP}(t)\right),$$

where X_r^{ENG} represents the previous ENG model recorded from a channel r (see "multiple biophysical source localization") without multiplicative noise and

$$g_\alpha(t) = \frac{X_\alpha(t) - \min X_\alpha(t)}{\max X_\alpha(t) - \min X_\alpha(t)} + \sigma_n, \ \alpha = BP, RESP$$

are stochastic time-dependent modulation factors simulating movement artifacts related to BP and RESP profiles, $X_\alpha(t)$. The deterministic numerical values of these modulation factors $g_\alpha(t)$ range from 0–1. We thus added a Gaussian noise $\sigma_n \sim N(0,\ 0.1)$ with variance equal to 10% of the maximal values of the deterministic part of $g_\alpha(t)$.

We added a spatial dependence of the motion-related artifacts by modeling a heterogenous effect on different channels. We considered a Lorentzian spatial distribution by means of the coefficients

$$\widehat{\beta}_{\alpha,r} = \frac{1}{1+d^2_{k_{\alpha,r}}},\ \textit{where}\ d_{k_{\alpha,r}} = (\theta_{k_\alpha} - \theta_r)\pi R,$$

where k_α is the index of the site where the contact impedance modulation correlated to function $\alpha = \{BP, RESP\}$ is maximal, θ_r is the angle expressed in radians of the channel r related to polar coordinates with origin in the center of the nerve section, and R is the radius of the nerve.

To limit the coefficient $\widehat{\beta}$ in the interval [0.1,1], we normalized them by means of the equation

$$\beta_{\alpha,j} = \frac{\widehat{\beta}_{\alpha,j} - \min\widehat{\beta}_\alpha}{\max\widehat{\beta}_\alpha - \min\widehat{\beta}_\alpha}\cdot(\beta_{\max} - \beta_{\min}) + \beta_{\min},$$

where

$$\beta_{\max} = 1$$
$$\beta_{\min} = 0.1.$$

We performed the same set of simulation as in multiple biophysical source localization.

Macroscopic physiological signal generation

To simulate macroscopic physiological signals like BP and RESP, we assumed to measure vital signals of a healthy individual in a resting state with a sampling frequency equal to 40 kHz to be consistent with neural signal frequency sampling ("generation of physiologically plausible neural recordings").

BP signal

The synthetic BP signal X^{BP} was generated using the dynamical system presented previously,[29] which we report in the supplemental experimental procedures. The heart rate (HR) was imposed equal to 75 beats per minute (bpm) because it is the average value for a healthy subject at rest.[30] We hypothesized that, during rest, the sympathetic and parasympathetic activities modulating the HR equilibrated, which is reflected in the choice of setting $\sigma_1^2/\sigma_2^2 = 0.5$ (see supplemental experimental procedures for further information).

RESP signal

The synthetic RESP signal X^{RESP} (Figure 7A) was generated using a simple resistive-capacitive (RC) model[31] (see supplemental experimental procedures for more information). The RESP cycle duration was imposed to be 3.75 s (1.00 s inspiration, 2.75 s expiration), whereas other parameters have been set to have a tidal volume (TV) of around 0.45 L during the inspiration peaks, corresponding to the average standard rest condition. The phase of the signal was adjusted to align the inspiratory peaks with the oscillations due to RESP sinus arrhythmia.

Generation of physiologically plausible neural recordings

For each nerve section, we populated half of the fascicles with Aβ fibers and the remaining fascicles with Aα fibers (Figure S2), this approximately respects the proportion between afferent and efferent fascicles observed in functional vagotopy.[8,11] To respect the proportion of fibers from the two populations observed physiologically, but limiting computational effort, we imposed the average number of fibers per fascicle equal to a quarter of the true value (766 fibers/fascicle afferently and 335 fibers/fascicle efferently[11]), resulting in a fiber density equal to 1,367 fibers/mm^2 in the afferent fascicles and 598 fibers/mm^2 in the efferent ones. Fiber models were implemented in NEURON using Python. Aα motor and Aβ sensory fibers were modelled with Gaines' implementation[32] of the classic McIntyre-Richardson-Grill (MRG) fiber[33] (Figure 2A).

The MRG model of a myelinated fiber consists of a multi-compartment double cable in which each internodal section is composed of 2 paranodal myelin attachment segments (MYSA), 2 paranodal main segments (FLUT), and 6 internodal segments (STIN). In Figure S3A, the Gaines' implementation lumped-parameter equivalent circuit of internodal and nodal sections is reported.

For each node of each fiber, the membrane current density corresponding to a single action potential was recorded virtually using a time resolution equal to 5 μs, and then each signal was converted in a current scaling for the node's area and finally downsampled, achieving a sampling frequency of 40 kHz. A fiber segment with a length of 2 cm (Figure S3B) was modeled for each different value of the fiber diameter, which was sampled from a normal distribution $N(11.5\ \mu m, 2.2\ \mu m)$ truncated at [10,13] μm for Aα fibers and from a normal distribution $N(9\ \mu m, 2.8\ \mu m)$ for an Aβ fiber truncated at [6,12] μm for Aβ fibers. As in Smets et al.,[34] we modeled only myelinated fibers, and unmyelinated fibers (C fibers) were not considered. This is because the amplitude of an action potential (AP) is proportional to the square of the fiber diameter,[35] and because the diameter of the myelinated fibers is larger than that of the unmyelinated fibers, the amplitude of the APs of the myelinated fibers turns out to be larger, causing the unmyelinated fibers to have a less predominant contribution in an *in vivo* recording. To generate the synthetic ENG signal, we followed what has been done, for example, by Wodlinger and Durand[12] and Jehenne et al.[26] We determined the shapes $w_{f,r}(t)$ of the f-th fiber single-unit AP (SUAP) recorded by recording site r using the theoretical LFM and summing the contributions of the different nodes in each single fiber; i.e.,

$$w_{f,r}(t) = \sum_{n\in f} w_n(t) L_{n,r}.$$

We determined the spike times $\tau_f(t) \in \{0,\ 1\}$ (where the ones correspond to the peak of an AP) for each fiber f in the section (Figures 6B and 7B) and produced the signals at a given site because of any single fiber by convolving the array of its spike times with the SUAP recorded by that site; i.e.,

$$X^{ENG}_{f,r}(t) = w_{f,r}(t) \otimes \tau_f(t).$$

The signals recorded by the same site were finally summed up to produce the ENG recorded by that site,

$$X^{ENG}_{r}(t) = \sum_f X^{ENG}_{f,r}(t).$$

The shape of the characteristic SUAPs $w_{f,r}(t)$ was determined by adding up the membrane current from each fiber node, obtained after a short intracellular stimulation pulse with amplitude sufficient to elicit a single AP, scaled according to the resistance between the node and the recording site (Figure S3C). In this way, a different template for each recording channel and for each fiber was obtained (Figure S3D).

To compute the array of spike times $\tau_f(t)$ for each fiber, we assumed that two of the fascicles containing Aβ fibers were related to BP and RESP, respectively, and that all remaining fascicles were supposed to provide neural background noise. Refractory periods for all fibers were imposed equal to 1.5 ms by removing events with a smaller interspike interval.

The fiber spike times for the informative neural components (BP, RESP) were generated by an inhomogeneous Poisson processes with time-varying rates proportional to the values of simulated BP and ventilation airflow, obtained from the dynamic system from Clifford and McSharry[29] and the lumped parameters model,[31] respectively.

In particular, the two time series were rescaled between 2.5 and 25 Hz according to microneurographic signals from human VN,[21]

$$\lambda^{BP}(t) = X^{rBP}(t),\ \lambda^{RESP}(t) = X^{rRESP}(t),$$

where X^{rBP} and X^{rRESP} are the rescaled physiological signals. The spike trains for the noisy neural component were generated by homogeneous Poisson processes with randomly chosen rates between 2.5 and 25 Hz (one rate for one fiber).

The neural signal components modulating BP and RESP were generated by Aβ fibers,[19,20] as were the noisy neural signals from all fascicles except one, which was populated by Aα fibers, to respect a naturalistic proportion

of afferent versus efferent fibers in the nerve.[36] Finally, to have a direct comparison with real-data experiments, we estimated SNR measures following previous procedures[19,20] to extract BP and RESP profiles. The SNR was computed as the ratio between the maximum of BP and RESP and the baseline amplitude of the respective signals.

Statistical analysis

Comparisons between source localization error distributions and random localization

To determine the chance level for the localization errors, we computed the distribution of localization errors obtained by localization algorithm randomly placing the source inside the admissible subset of the nerve sections (the whole section excluding the electrode bodies for generic models, and the fascicular regions for structural models). We thus computed the distribution of localization errors by considering surrogate data generated using the corresponding synthetic data simulation setting. To compare the performance of random versus source localization algorithms, we used a Kolmogorov-Smirnov test followed by Bonferroni correction for multiple comparisons.

Comparisons between source localization algorithms, electrode types, and geometrical models

We employed GLMs for localization errors to estimate the effects of considering different localization algorithms, electrode types, and geometrical models.

We considered the three synthetic data simulation settings described above ("*in silico* experiments via discriminative indices"). We considered possible random effects because of multiple simulations for each nerve section and for each source distribution in the nerve fascicles.

The fixed effects common in all three synthetic data simulation settings were

- source localization algorithm: for deterministic sources (single and multiple sinusoidal sources) DFP, DBF and BF (reference level); for neural sources DBF and DFP (reference level);
- electrode type: cuff (reference level) or TIME;
- geometrical model: generic (reference level) or structural.

In the case of multiple deterministic sources, the frequency of the source of interest was added to the fixed effects. In the case of multiple neural sources, the physiological function related to the source is added to the fixed effects (BP or RESP, with BP reference level).

The random effects were the identifiers of nerve section and fascicle containing the informative source. Because fascicles in different sections have different sets of identifiers, fascicles and section identifiers are nested random effects.

Because localization errors are positive definite, we employed a gamma distribution with link function x^{-1}. Namely, the errors for a given choice of the fixed effect factors are distributed according to a gamma distribution $\Gamma(\lambda_{error})$; i.e.,

$$(\lambda_{\text{error}})^{-1} \sim \beta_{\text{DBF}} X_{DBF} + (\beta_{DFP} X_{DFP}) + \beta_{TIME} X_{TIME} + \beta_{struct} X_{struct} + (\beta_{freq} X_{freq}) + (\beta_{RESP} X_{RESP}) + \varepsilon + b_{sect} + b_{fasc\,|\,sect},$$

where we put in parentheses the terms that can be omitted depending on the experimental settings. The random terms are $\varepsilon \sim N(0, \sigma_\varepsilon)$, $b_{sect} \sim N(0, \sigma_{sect})$, and $b_{fasc\,|\,sect} \sim N(0, \sigma_{fasc\,|\,sect})$.

When a factor is categorical, a reference level is established, and a term of the above expansion is added for each different level ℓ. The corresponding X_ℓ is 1 when the factor occurs at level ℓ and 0 otherwise. At the reference level, all X_ℓ corresponding to a factor are 0.

Because the fixed effects determine the reciprocal of the average localization error, positive values fixed effects β_X decrease the characteristic error, and negative fixed effects increase it. High absolute value fixed effects have a stronger effect on the error in both directions.

SUPPLEMENTAL INFORMATION

Supplemental information can be found online at https://doi.org/10.1016/j.patter.2022.100615.

ACKNOWLEDGMENTS

This work was partly funded by the Bertarelli Foundation and by the EU project NeuHeart.

AUTHOR CONTRIBUTIONS

Conceptualization, A.P., S.R., F.V., and S.M.; methodology, A.P., S.R., and F.V.; software, A.P. and S.R.; formal analysis, A.P. and S.R.; writing – original draft, A.P., S.R., and F.V.; writing – review & editing, A.P., S.R., F.V., and S.M.; visualization, A.P.; supervision, F.V. and S.M.; funding acquisition, S.M.

DECLARATION OF INTERESTS

S.M. is a founder and shareholder of Sensars Neuroprosthetics Sarl, a start-up company that could benefit from the methods in this work. A.P., S.R., F.V., and S.M. are inventors of a pending patent application concerning the methods in this work.

Received: June 9, 2022
Revised: July 8, 2022
Accepted: September 29, 2022
Published: October 31, 2022

REFERENCES

1. Birmingham, K., Gradinaru, V., Anikeeva, P., Grill, W.M., Pikov, V., McLaughlin, B., Pasricha, P., Weber, D., Ludwig, K., and Famm, K. (2014). Bioelectronic medicines: a research roadmap. Nat. Rev. Drug Discov. *13*, 399–400. https://doi.org/10.1038/nrd4351.
2. Cracchiolo, M., Ottaviani, M.M., Panarese, A., Strauss, I., Vallone, F., Mazzoni, A., and Micera, S. (2021). Bioelectronic medicine for the autonomic nervous system: clinical applications and perspectives. J. Neural. Eng. *18*, 041002. https://doi.org/10.1088/1741-2552/abe6b9.
3. Karemaker, J.M. (2017). An introduction into autonomic nervous function. Physiol. Meas. *38*, R89–R118. https://doi.org/10.1088/1361-6579/aa6782.
4. Fitchett, A., Mastitskaya, S., and Aristovich, K. (2021). Selective neuromodulation of the vagus nerve. Front. Neurosci. *15*, 685872. https://doi.org/10.3389/fnins.2021.685872.
5. Tosato, M., Yoshida, K., Toft, E., and Struijk, J.J. (2007). Quasi-trapezoidal pulses to selectively block the activation of intrinsic laryngeal muscles during vagal nerve stimulation. J. Neural. Eng. *4*, 205–212. https://doi.org/10.1088/1741-2560/4/3/005.
6. Patel, Y.A., and Butera, R.J. (2015). Differential fiber-specific block of nerve conduction in mammalian peripheral nerves using kilohertz electrical stimulation. J. Neurophysiol. *113*, 3923–3929. https://doi.org/10.1152/jn.00529.2014.
7. Vuckovic, A., Tosato, M., and Struijk, J.J. (2008). A comparative study of three techniques for diameter selective fiber activation in the vagal nerve: anodal block, depolarizing prepulses and slowly rising pulses. J. Neural. Eng. *5*, 275–286. https://doi.org/10.1088/1741-2560/5/3/002.
8. Settell, M.L., Pelot, N.A., Knudsen, B.E., Dingle, A.M., McConico, A.L., Nicolai, E.N., Trevathan, J.K., Ezzell, J.A., Ross, E.K., Gustafson, K.J., et al. (2020). Functional vagotopy in the cervical vagus nerve of the domestic pig: implications for the study of vagus nerve stimulation. J. Neural. Eng. *17*, 026022. https://doi.org/10.1088/1741-2552/ab7ad4.
9. Pelot, N.A., Goldhagen, G.B., Cariello, J.E., Musselman, E.D., Clissold, K.A., Ezzell, J.A., and Grill, W.M. (2020). Quantified morphology of the cervical and Subdiaphragmatic vagus nerves of human, pig, and rat. Front. Neurosci. *14*, 601479. https://doi.org/10.3389/fnins.2020.601479.
10. Aristovich, K., Donega, M., Fjordbakk, C., Tarotin, I., Chapman, C.A.R., Viscasillas, J., Stathopoulou, T.-R., Crawford, A., Chew, D., Perkins, J., and Holder, D. (2021). Model-based geometrical optimisation and *in vivo* validation of a spatially selective multielectrode cuff array for vagus nerve neuromodulation. J. Neurosci. Methods *352*, 109079. https://doi.org/10.1016/j.jneumeth.2021.109079.

11. Jayaprakash, N., Toth, V., Song, W., Vardhan, A., Levy, T., Tomaio, J., Qanud, K., Mughrabi, I., Saperstein, Y., Chang, Y.-C., et al. (2022). Organ- and function-specific anatomical organization and bioelectronic modulation of the vagus nerve. Preprint at Cell Press Sneak Peek. https://doi.org/10.2139/ssrn.4097124.

12. Wodlinger, B., and Durand, D.M. (2009). Localization and Recovery of peripheral neural sources with beamforming algorithms. IEEE Trans. Neural Syst. Rehabil. Eng. *17*, 461–468. https://doi.org/10.1109/TNSRE.2009.2034072.

13. Zariffa, J., and Popovic, M.R. (2009). Localization of active Pathways in peripheral nerves: a simulation study. IEEE Trans. Neural Syst. Rehabil. Eng. *17*, 53–62. https://doi.org/10.1109/TNSRE.2008.2010475.

14. Eggers, T.E., Dweiri, Y.M., McCallum, G.A., and Durand, D.M. (2017). Model-based Bayesian signal extraction algorithm for peripheral nerves. J. Neural. Eng. *14*, 056009. https://doi.org/10.1088/1741-2552/aa7d94.

15. Vallone, F., Ottaviani, M.M., Dedola, F., Cutrone, A., Romeni, S., Panarese, A.M., Bernini, F., Cracchiolo, M., Strauss, I., Gabisonia, K., et al. (2021). Simultaneous decoding of cardiovascular and respiratory functional changes from pig intraneural vagus nerve signals. J. Neural. Eng. *18*, 0460a2. https://doi.org/10.1088/1741-2552/ac0d42.

16. Ravagli, E., Mastitskaya, S., Thompson, N., Iacoviello, F., Shearing, P.R., Perkins, J., Gourine, A.V., Aristovich, K., and Holder, D. (2020). Imaging fascicular organization of rat sciatic nerves with fast neural electrical impedance tomography. Nat. Commun. *11*, 6241. https://doi.org/10.1038/s41467-020-20127-x.

17. Thompson, N., Ravagli, E., Mastitskaya, S., Iacoviello, F., Perkins, J., Shearing, P., Aristovich, K., and Holder, D. (2022). Fascicular Organisation and Neuroanatomy of the Porcine and human vagus nerves: allowing for spatially selective vagus nerve stimulation. Faseb. J. *36*. https://doi.org/10.1096/fasebj.2022.36.S1.R3366.

18. Boretius, T., Badia, J., Pascual-Font, A., Schuettler, M., Navarro, X., Yoshida, K., and Stieglitz, T. (2010). A transverse intrafascicular multichannel electrode (TIME) to interface with the peripheral nerve. Biosens. Bioelectron. *26*, 62–69. https://doi.org/10.1016/j.bios.2010.05.010.

19. Sevcencu, C., Nielsen, T.N., and Struijk, J.J. (2017). A neural blood pressure marker for bioelectronic medicines for treatment of hypertension. Biosens. Bioelectron. *98*, 1–6. https://doi.org/10.1016/j.bios.2017.06.031.

20. Sevcencu, C., Nielsen, T.N., Kjærgaard, B., and Struijk, J.J. (2018). A respiratory marker derived from left vagus nerve signals recorded with implantable cuff electrodes. Neuromodulation *21*, 269–275. https://doi.org/10.1111/ner.12630.

21. Ottaviani, M.M., Wright, L., Dawood, T., and Macefield, V.G. (2020). *In vivo* recordings from the human vagus nerve using ultrasound-guided microneurography. J. Physiol. *598*, 3569–3576. https://doi.org/10.1113/JP280077.

22. Settell, M.L., Skubal, A.C., Chen, R.C.H., Kasole, M., Knudsen, B.E., Nicolai, E.N., Huang, C., Zhou, C., Trevathan, J.K., Upadhye, A., et al. (2021). *In vivo* Visualization of pig vagus nerve "vagotopy" using ultrasound. Front. Neurosci. *15*, 676680. https://doi.org/10.3389/fnins.2021.676680.

23. Romeni, S., Valle, G., Mazzoni, A., and Micera, S. (2020). Tutorial: a computational framework for the design and optimization of peripheral neural interfaces. Nat. Protoc. *15*, 3129–3153. https://doi.org/10.1038/s41596-020-0377-6.

24. Dali, M., Rossel, O., Andreu, D., Laporte, L., Hernández, A., Laforet, J., Marijon, E., Hagège, A., Clerc, M., Henry, C., and Guiraud, D. (2018). Model based optimal multipolar stimulation without a priori knowledge of nerve structure: application to vagus nerve stimulation. J. Neural. Eng. *15*, 046018. https://doi.org/10.1088/1741-2552/aabeb9.

25. Grinberg, Y., Schiefer, M.A., Tyler, D.J., and Gustafson, K.J. (2008). Fascicular perineurium thickness, size, and position affect model predictions of neural Excitation. IEEE Trans. Neural Syst. Rehabil. Eng. *16*, 572–581. https://doi.org/10.1109/TNSRE.2008.2010348.

26. Jehenne, B., Raspopovic, S., Capogrosso, M., Arleo, A., and Micera, S. (2015). Recording properties of an electrode implanted in the peripheral nervous system: a human computational model. In 2015 *7th International IEEE/EMBS Conference on Neural Engineering (NER)*, pp. 482–485. https://doi.org/10.1109/NER.2015.7146664.

27. Bossetti, C.A., Birdno, M.J., and Grill, W.M. (2008). Analysis of the quasi-static approximation for calculating potentials generated by neural stimulation. J. Neural. Eng. *5*, 44–53. https://doi.org/10.1088/1741-2560/5/1/005.

28. Babiloni, F., Babiloni, C., Carducci, F., Romani, G.L., Rossini, P.M., Angelone, L.M., and Cincotti, F. (2003). Multimodal integration of high-resolution EEG and functional magnetic resonance imaging data: a simulation study. Neuroimage *19*, 1–15. https://doi.org/10.1016/S1053-8119(03)00052-1.

29. Clifford, G.D., and McSharry, P.E. (2004). A realistic coupled nonlinear artificial ECG, BP, and respiratory signal generator for assessing noise performance of biomedical signal processing algorithms. In Proc. SPIE 5467, Fluctuations and Noise in Biological, Biophysical, and Biomedical Systems II. https://doi.org/10.1117/12.544525.

30. Nanchen, D. (2018). Resting heart rate: what is normal? Heart *104*, 1048–1049. https://doi.org/10.1136/heartjnl-2017-312731.

31. Plummer, A.R., du Bois, J.L., Flynn, J.M., Roesner, J., Lee, S.M., Magee, P., Thornton, M., Padkin, A., and Gill, H.S. (2020). A simple method to estimate flow restriction for dual ventilation of dissimilar patients: the BathRC model. PLoS One *15*, e0242123. https://doi.org/10.1371/journal.pone.0242123.

32. Gaines, J.L., Finn, K.E., Slopsema, J.P., Heyboer, L.A., and Polasek, K.H. (2018). A model of motor and sensory axon activation in the median nerve using surface electrical stimulation. J. Comput. Neurosci. *45*, 29–43. https://doi.org/10.1007/s10827-018-0689-5.

33. McIntyre, C.C., Richardson, A.G., and Grill, W.M. (2002). Modeling the excitability of mammalian nerve fibers: Influence of Afterpotentials on the Recovery cycle. J. Neurophysiol. *87*, 995–1006. https://doi.org/10.1152/jn.00353.2001.

34. Smets, H., Stumpp, L., Julémont, N., Cury, J., Debelle, A., Innocenti, B., Vespa, S., Haut, B., Doguet, P., Vanhoestenberghe, A., et al. (2021). Analysing vagus nerve spontaneous activity using finite element modelling. J. Neural. Eng. *18*, 056008. https://doi.org/10.1088/1741-2552/abe68f.

35. Stein, R.B., and Pearson, K.G. (1971). Predicted amplitude and form of action potentials recorded from unmyelinated nerve fibres. J. Theor. Biol. *32*, 539–558. https://doi.org/10.1016/0022-5193(71)90155-X.

36. Agostoni, E., Chinnock, J.E., Daly, M.D.B., and Murray, J.G. (1957). Functional and histological studies of the vagus nerve and its branches to the heart, lungs and abdominal viscera in the cat. J. Physiol. *135*, 182–205. https://doi.org/10.1113/jphysiol.1957.sp005703.